Surface Oxygen Vacancy Formation Energy Calculations in 34 Orientations of β-Ga_2O_3 and θ-Al_2O_3

Yoyo Hinuma[1,2*], Takashi Kamachi[3,4], Nobutsugu Hamamoto[3], Motoshi Takao[5], Takashi Toyao[4,5], and Ken-ichi Shimizu[4,5]

[1] Center for Frontier Science, Chiba University, 1-33 Yayoicho, Inage, Chiba 263-8522, Japan

[2] Center for Materials Research by Information Integration, Research and Services Division of Materials Data and Integrated System, National Institute for Materials Science, 1-2-1 Sengen, Tsukuba, Ibaraki 305-0047, Japan

[3] Department of Life, Environment and Applied Chemistry, Fukuoka Institute of Technology, 3-30-1Wajiro-Higashi, Higashi-ku, Fukuoka 811-0295, Japan

[4] Elements Strategy Initiative for Catalysts and Batteries, Kyoto University, Kyoto University Katsura, Nishikyo-ku, Kyoto 615-8520, Japan

[5] Institute for Catalysis, Hokkaido University, N-21, W-10, Kita, Sapporo, Hokkaido 001-0021, Japan

* yoyo.hinuma@gmail.com

Abstract

Computational exploration of previously unknown reactive sites is a powerful strategy for emergence of new catalytic reactions. Exotic surfaces can be theoretically investigated, but there are very few, if any, computational models of high index orientations that considers reconstruction of the surface. A workflow to efficiently obtain a set of accessible terminations by removing those that are metastable against macroscopic facet formation and by comparing cleaved surfaces and surfaces suggested by a genetic algorithm (GA) for promising orientations is proposed and demonstrated using 34 orientations of β-Ga_2O_3 and θ-Al_2O_3. Seven and six terminations considered experimentally accessible are found for β-Ga_2O_3 and θ-Al_2O_3, respectively, where the highest surface energy was roughly twice of the lowest. The lowest surface O vacancy formation energy (E_{Ovac}) in an accessible surface is 3.04 and 5.46 eV in the (101) and (20$\bar{1}$) terminations for β-Ga_2O_3 and θ-Al_2O_3, respectively, where the decrease in E_{Ovac} from the most stable surface is 1.32 and 1.11 eV, respectively. The E_{Ovac} in accessible surfaces showed a good correlation with descriptors of the local coordination environment, suggesting that exploiting surface O in an unfavorable environment in an accessible termination would enhance O vacancy-related catalyst performance even in materials that do not show reactivity on the most stable surface.

1. Introduction

High catalytic reactivity in oxides are expected in high index surfaces and at surface defects, such as corners and step edges, since there are cations and anions with more unfavorable coordination environments including low coordination number. Theoretical studies are leading experimental investigations on irregular sites because of the difficulty of the latter. A pioneering computational work is first principles calculations on explicit models of step edges on the (101) surfaces of tetragonal ZrO_2 [1-2] and anatase TiO_2 [2]. Many orientations can be exposed on an actual oxide particle, thus development of an algorithm that can rapidly model diverse surfaces considering surface reconstruction would be very helpful. This is because attempts to experimentally synthesize high index surfaces and unstable surface sites, which can be handled in theoretical studies, could fail because of reconstruction to a stable surface. The reconstruction of ZnO (0001) and (000 $\overline{1}$) surfaces (*c*-plane) are thoroughly investigated, both experimentally and theoretically[3-7], while there is a detailed computational work on orthorhombic perovskite $LaFeO_3$ [8]. These ZnO surfaces as well as $LaFeO_3$ surfaces are polar, where the macroscopic dipole moment perpendicular to the surface plane diverges when considered as a function of system thickness [9-10]. Polar surfaces are often complicated because a compensating electric field is required to resolve this intrinsic so-called “polar instability”. Examples are through (1) intrinsic surface charge modification by partial filling of electronic states, (2) intrinsic or extrinsic modification of the surface region composition, or (3) extrinsic adsorption of charged foreign species. Although polar surfaces show a rich variety of reconstruction, the polar instability resolution mechanism strongly depends on the surface and therefore are not suitable when trying to screen many surfaces.

Defects strongly affect the chemistry and physics of metal oxides[11-14]. Catalytic, electrical, optical, and mechanical properties, as well as chemical reactivity, is typically governed by defects, both point and extended[15-19]. Among these, surface point defects of metal oxides, such as O vacancies, have a dominant effect on heterogeneous catalysis[20-22]. As an example, the Mars-Van Krevelen mechanism is a prototypical catalytic process where the reaction sites are surface O vacancies on a metal oxide catalyst.[23-26] The surface O desorption energy (E_{Ovac}), which is equivalent to the surface O vacancy formation energy, is a physical quantity that reasonably predict catalytic performance in relevant catalytic processes[27-28].

Many experimental methods are used to investigate O vacancies[29-31]. Scanning probe techniques are especially useful and successfully revealed much information regarding

the structure of surfaces with defects[32-35]. However, there is much uncharted territory in experimental observation of O vacancies because evaluation of E_{Ovac} is not always possible even when employing sophisticated techniques[36]. In contrast, there are recent theoretical studies on O vacancies of metal oxides[37-41], which are very important because surface defect sites are often adsorption sites and the adsorption process is a key step for many surface-catalyzed reactions[42-43]. Finding good correlations between properties that are hard to obtain, such as E_{Ovac}, and properties easy to obtain, where examples are the band gap (BG), bulk formation energy (E_{form}), and ionization potential (IP), is important in two aspects. First, these relations often provide insight on the science that governs the former property. Second, screening of candidate materials can be accelerated. Suppose we want materials where some property lies within a desirable range. One example is a catalyst candidate where E_{Ovac} is close to a certain value. Searching of useful materials can be accelerated by investigating latter properties ("descriptors" in the language of materials informatics) at low cost and then removing materials that are unlikely to have a desirable E_{Ovac}. The main descriptors of E_{Ovac} for relatively stable surfaces are the bulk minimum BG and E_{form}[28], which are similar to descriptors for neutral O vacancy formation energies in bulk[44]. However, the surface termination dependence on E_{Ovac} has not been investigated in detail.

This research calculates E_{Ovac} of different surface terminations in a given crystal. In particular, discovery of a strategy to find highly reactive sites in synthesizable surfaces with surface energy (E_{surf}) higher than the most stable surface could lead to emergence of previously untapped reactivity in already known materials. 67 terminations each of β-Ga_2O_3 and θ-Al_2O_3 are initially investigated on an equal computation level. These isostructural materials have low symmetry (space group symbol *C*2/*m*) and, therefore, many slab models with different orientations can be obtained for a given supercell size limit compared to high symmetry structures. These materials are also industrially important. β-Ga_2O_3 has been widely used in electronics and optoelectronics[45-46], namely as an *n*-type widegap semiconductor for solar-blind UV detectors [47-48], gas sensors [49-50], and transparent conductors[51-52]. Recently, the possibility of relatively cost-effective device fabrication as well as the high Baliga's (specific on-resistance in vertical drift region) and Johnson's (power-frequency capability) figures of merit, have been attracting significant research interest in power device applications [53-54]. β-Ga_2O_3 also demonstrates catalytic activity. For example, β-Ga_2O_3 is experimentally found to split water[55], and computational studies indicate that β-Ga_2O_3 is active in CO_2 hydrogenation[56] and that excess electrons from neutral O vacancies affect the activation energy for oxygen

evolution reaction intermediates [57]. Al_2O_3 has many polymorphs including α (corundum), θ, δ, κ, γ, χ, and η[58-59]. The θ phase is a relatively stable polymorph that requires 1000 to 1200 °C to cause a phase transition to the stable α phase. The γ phase is frequently used in catalysis. Atomically-dispersed noble metal catalysts, so-called single-atom catalysts, supported on Al_2O_3 have been synthesized for CO [60-62] and NO [63] conversion reactions. In addition, non-oxidative isobutene dehydrogenation has been reported on Al_2O_3 [64]. Although the θ phase is not actively considered as a catalyst, careful engineering of the surface based on theoretical insights may bring about emergence of new reactivity. A direct comparison with In_2O_3 would be attractive in the scope of this study. Heavily doped *n*-type In_2O_3, where Sn is commonly used as the dopant, is a prototypical transparent conductive oxide for electrode applications [65-67]. Gas sensing of both oxidizing gases, including NO_2, NO, and SO_2, and reducing gases, for instance H_2, CO, and propane, is possible by doping to change the surface oxidation state[68]. In_2O_3 also has many uses in catalysis. Pure In_2O_3 can promote hydrogenation of CO_2 to CH_3OH[69-71], and the performance can be improved by combining with, for example, Pd[72-73] and ZrO_2[74]. Pd-doped In_2O_3 can also hydrogenate amides to form amines and alcohols[75]. Unfortunately, In_2O_3 cannot take the β-Ga_2O_3 structure[76], and therefore it is not considered in this paper.

2. Methodology

First-principles calculations were conducted using the projector augmented-wave method[77] as implemented in the VASP code[78-79]. As in our previous study[28], the Perdew-Burke-Ernzerhof functional tuned for solids (PBEsol) [80] within the generalized gradient approximation (GGA) was used because it provides reasonable bulk energetics and crystal structures, for instance, compared to the standard PBE-GGA functional [81] as shown in a previous systematic study of groups I to VI binary oxides [82]. A comparison of relative energies between the PBE-GGA, the strongly constrained and appropriately normed (SCAN) meta-GGA [83], and Heyd-Scuseria-Ernzerhof (HSE06) range-separated hybrid [84-86] functionals for polymorphs of Ga_2O_3 is available in Ref. [76]. The PBEsol direct and minimum band gaps are 1.98 and 2.03 eV for β-Ga_2O_3 and 4.54 and 4.83 eV for θ-Al_2O_3, respectively. The experimental band gap is 4.7[87] or 4.9 eV [88] for β-Ga_2O_3 and 7.4 eV [89] for θ-Al_2O_3, hence the band gap underestimation in PBEsol is about 3 eV in both compounds. The PBE band gap, both minimum and direct, is smaller than PBEsol by 0.2 and 0.1 eV for β-Ga_2O_3 and θ-Al_2O_3, respectively, showing that the underestimation is slightly more significant in PBE compared to PBEsol.

Slab-and-vacuum models under three-dimensional periodic boundary conditions

(hereafter simply “slab models”) were used to analyze surfaces, where slabs infinitely extending parallel to the *ab*-plane alternate with vacuum layers along the *c*-axis. Initial models were obtained by simply cleaving bulk. The considered surfaces are type 2 in Tasker’s definition[90], or nonpolar type B in the definition by Hinuma *et al.*[91], except for the (010) surface that is Tasker type 1 and nonpolar type A, respectively. Two distinct terminations exist for each orientation except for the (010) surface where only one exist. The in-plane area is defined as the minimum possible area in the *ab*-plane allowed for a slab model. Slab models with an in-plane area less than four times that of the smallest possible in-plane area were considered. 67 terminations each were obtained for both β-Ga_2O_3 and θ-Al_2O_3. The geometries of adopted models are given in Tables S1 and S2, respectively, and the terminations are illustrated in Figures S1-S9. Internal coordinates and lattice parameters were relaxed in bulk calculations, and all internal coordinates were allowed to relax while lattice parameters were fixed in slab model calculations.

The surface energy, E_{surf}, is defined as

$$E_{\text{surf}} = \left(E_{\text{slab}} - E_{\text{bulk}}\right)/2A, \qquad (1)$$

where E_{slab} and E_{bulk} are the energy of the slab without defects and the energy of the constituents of the slab when in a perfect bulk, respectively. A is the in-plane area of the slab, where the coefficient of 2 accounts for both sides of the slab. The most natural choice of E_{bulk} is from a bulk calculation, and this is used for E_{slab} in “thin” and “thick” slabs in Supplementary Tables SI-3 and SI-4. The difference in E_{slab} and the IP between “thin” and “thick” slabs defined in Supplementary Tables SI-1 and SI-2 is less than 5 meV/Å^2 and 0.15 eV, respectively. The E_{surf} and IP reflect the arrangement of atoms and the charge distribution at the surface. These quantities, which are easy to obtain, are used to check the convergence of the slab with respect to the slab thickness. The E_{surf} where E_{bulk} is based on a linear fit of energies from these slabs (see Ref. [28] for details) is given in the “fit” column. Namely, the fitted surface energy is

$$E_{\text{surf}}^{\text{fit}} = \left(n_{\text{thick}} E_{\text{surf}}^{\text{thin}} - n_{\text{thin}} E_{\text{surf}}^{\text{thick}}\right)/\left(n_{\text{thick}} - n_{\text{thin}}\right) \qquad (2)$$

where $E_{\text{surf}}^{\text{thin}}$ and $E_{\text{surf}}^{\text{thick}}$ are the E_{surf} of thin and thick slabs, respectively, while n_{thick} and n_{thin} are the number of atoms in the thin and thick slabs, respectively, with a common in-plane area. This fitted definition of E_{surf} is used in subsequent analysis unless otherwise noted. The IP is based on the bulk-based definition in Hinuma et al.[92] The relative differences between terminations in the IP, the electron affinity (EA), and the

work function when defined as the mean of the IP and EA are the same because the difference between the IP and EA is always the bulk band gap (BG) that is a constant for each compound in this definition. Only relative differences between terminations for the same compound is relevant in this study, thus only the IP is considered. The O vacancy formation energy is defined as

$$E_{\mathrm{Ovac}} = \left(E_{\mathrm{removed}} - E_{\mathrm{slab}} + 2\mu_O\right)/2 \qquad (3)$$

where E_{removed} and μ_O are the energy of the slab when two O atoms are removed (one O from each surface) and the chemical potential of the O (that of O_2 gas in this study), respectively.

3. Results and discussion

3.1. Finding reasonable terminations

Correlations between the minimum E_{Ovac} and a number of descriptors were obtained for β-Ga_2O_3 and θ-Al_2O_3. The E_{Ovac} of stable surfaces of binary oxides is strongly related to the bulk BG and E_{form} [28], while the O vacancy formation energy bulk correlates with the BG, enthalpy of formation, midgap energy relative to the O 2*p* band center, and the atomic electronegativities[44, 93]. However, these descriptors cannot be used when investigating different terminations of the same crystal. Three descriptors were examined instead, which are the E_{surf}, IP, and BG of the slab model. The coefficient of determination (R^2) and root mean square error (RMSE) of the linear fit are shown in Table 1. Here, terminations with $E_{\mathrm{Ovac}}<0$ were removed from consideration. Plots of the minimum E_{Ovac} for each surface versus E_{surf}, which had the best R^2 among the three descriptors in both compounds, are shown in Fig. 1 using circles and triangles. E_{Ovac} decreases with increasing E_{surf}, which is natural because less stable surfaces could have O in less favorable environments that can be removed with lower energy. The RMSEs are 0.70 and 0.80 eV for β-Ga_2O_3 and θ-Al_2O_3, respectively. These values are very bad for a good reason. Points with large E_{surf} strongly tend to lie below the linear fit in Fig. 1, which means that using a linear fit is not suitable when trying to reduce the RMSE. Terminations that were relaxed with first principles calculations after simply cleaving from bulk could have extremely high E_{surf}, and defect formation, such as removal of O from the surface, may spontaneously cause relaxation that drastically reduces the surface energy. The effect of this relaxation results in a very low E_{Ovac} that could even become negative in some cases. In other words, inclusion of surfaces that are very unrealistic, which is the case in some cleaved surfaces, corrupts the veracity of the data. To increase the volume and

variety of the data without compromising veracity, surfaces that are appropriately reconstructed need to be added. From another viewpoint, terminations that are likely to be experimentally accessible need to be distinguished from those that are not because only surfaces that can be experimentally synthesized, preferably with less effort, can be used industrially and therefore contribute to improvement of our society. We propose the following workflow to find a set of reasonable terminations while keeping computational costs low. A flow chart is provided in Fig. 2.

Table 1. R^2 and RMSE of linear fits of E_{Ovac} for slabs cleaved from bulk.

	β-Ga_2O_3			θ-Al_2O_3		
	E_{surf}	IP	BG	E_{surf}	IP	BG
R^2	0.39	0.02	0.08	0.47	0.06	0.40
RMSE	0.70	0.89	0.86	0.80	1.07	0.86

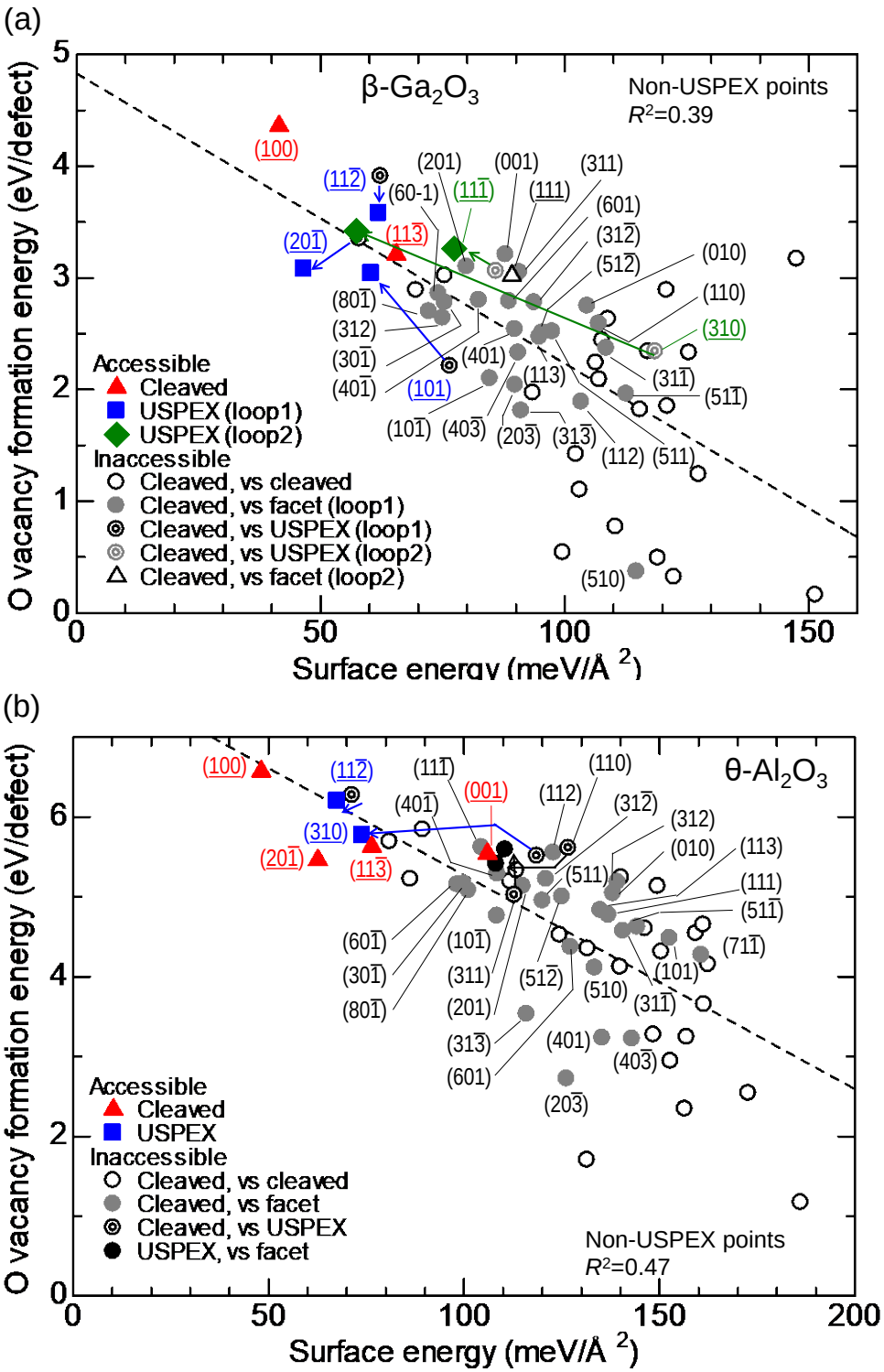

Fig. 1. E_{Ovac} vs E_{surf} for (a) β-Ga_2O_3 and (b) θ-Al_2O_3. Accessible surfaces are shown in colored pointed symbols. Inaccessible surfaces are shown in black or gray symbols, and the symbol depends on the type of competing surface. The R^2 for a linear fit of all non-USPEX terminations, including all inaccessible surfaces with a positive E_{Ovac}, is also given.

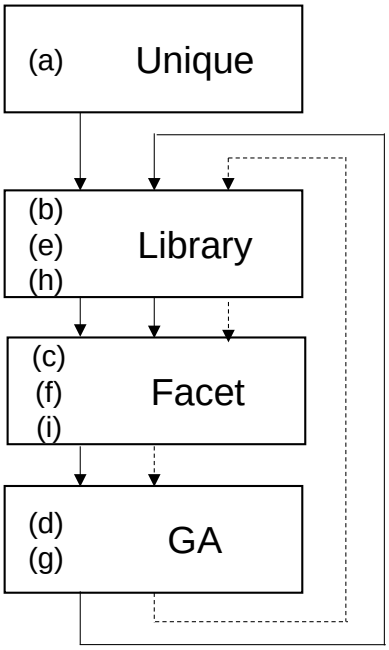

Fig. 2. Flowchart of termination search. Solid and dashed lines indicate the first and second loops, respectively.

[Loop 1]

(a) For each orientation, terminations where the E_{surf} is not the lowest are removed from consideration.

(b) A table of E_{surf} for each orientation (E_{surf} library) is prepared.

(c) Terminations that can lower E_{surf} by forming macroscopic facets are identified using the E_{surf} library.

(d) The most stable termination for orientations where macroscopic facet formation does not result in a lower E_{surf} is searched using a GA.

(e) The E_{surf} library is updated to reflect lowering of E_{surf} from GA calculations.

(f) Same as step (c).

[Loop 2]

(g) Additional GA calculations are conducted for terminations where the macroscopic facets that minimize the E_{surf} are both (1) at a large angle with respect to the original surface and (2) macroscopic facet formation reduces E_{surf} by a relatively small amount.

(h) Same as step (e).

(i) Same as step (f).

The goal of step (a) is to obtain the lowest E_{surf} for each orientation. In other words, a unique E_{surf} is assigned to each orientation, thereby the word "Unique" is used to represent this step in Fig. 2. All orientations except (010) have two terminations in this study, thus the termination with higher E_{surf} was removed from further consideration. For example, the (100)A termination of β-Ga_2O_3 has a lower E_{surf} than (100)B (see Supplementary Table SI-3), thus the (100)A termination was considered for the (100) orientation. The E_{surf} for each orientation is saved as a library in step (b), which is shown as "Library" in Fig. 2.

Reduction of E_{surf} through macroscopic facet formation is explored in the subsequent step (c) ("Facet" in Fig. 2). For a given surface with surface energy E_{surf0}, two surfaces at angles of θ_1 and θ_2 against the original surface are considered that have surface energies E_{surf1} and E_{surf2}, respectively [Fig. 3(a)]. Formation of macroscopic facets will reduce the surface energy if

$$E_{surf\,0} > \frac{E_{surf\,1}\sin\theta_2 + E_{surf\,2}\sin\theta_1}{\sin\left(\theta_1+\theta_2\right)} \qquad (4)$$

This relation is purely based on geometry and does not consider how atoms arrange at the edges of the facets. The effect of edges will be diminished if the facet width becomes wide enough (macroscopic facets) but cannot be ignored for narrow facets (microscopic facets). The algorithm to automatically find facet orientation pairs in Ref. [94] was used to find the lowest energy.

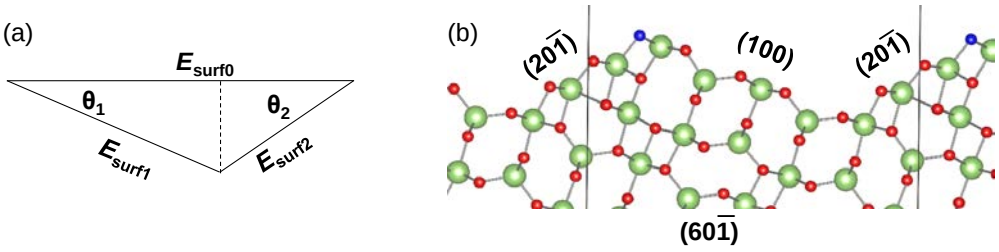

Fig. 3. (a) Geometry of a facet. (b) USPEX optimized surface of the β-Ga_2O_3 $(60\,\bar{1})$ orientation. Green and red balls indicate Ga and O, respectively. E_{Ovac} is minimized by removing the blue O site.

There is a need to confirm that the currently available termination is indeed reasonable for the orientation. Evolutionary algorithms are, along other fields, used in materials

discovery and optimization [95-107], and has been used to explore the surface of oxides. GA has been applied to oxides to determine the structure of TiO_2 [108]and MgO [109] nanoparticles. The advent of surface determination of a given orientation by GA using the USPEX code[95-98] led to studies of rutile-like RuO_2 (110)[110] and four SiO_2 surfaces[111]. In this study, GA calculations using USPEX were conducted on orientations where the E_{surf} does not decrease by macroscopic facet formation, which is step (d) in the flowchart ("GA" in Fig. 2).

To reduce computational cost, the General Utility Lattice Program (GULP) code [112-113] with interatomic potentials by Matsui [114] or Minervini et al.[115] was used as the energy calculator in USPEX. Detailed parameters of USPEX calculations are given in Supplementary Information 2. As of time of writing, USPEX calculates slabs where the atoms in the bottom part is fixed and the top part is not. One challenge of step (d) is to obtain a nonpolar slab model with a USPEX-determined termination. The E_{surf} of a slab is well-defined only if both surfaces are equivalent, or in other words, the slab is strictly nonpolar due to existence of a certain type of symmetry. Otherwise, only the sum (or mean average) of surface energies of the two surfaces is well-defined; the individual surface energies are unavailable. The surface energy of the termination from USPEX may be mathematically calculated by subtracting the surface energy of the non-relaxed termination, which can be obtained separately using a nonpolar slab, from the total surface energy of the slab. However, the energy of the slab would naturally depend on the number of atoms that could be relaxed; relaxation of more atoms will decrease the energy of the slab and therefore result in a smaller surface energy. The surface energy obtained using this procedure will be useful as a guide to determine the stability between terminations of USPEX slabs derived under the same conditions, and this is exactly why such energies can be used to compare the fitness between individuals in a GA. However, the energies lack the precision for detailed analysis between different orientations that is necessary in the proposed algorithm. This study used a procedure to construct a strictly nonpolar slab by carefully positioning the inversion center during USPEX calculations and then doubling the slab thickness (see Supplementary Information 2 for details). The internal coordinates of the nonpolar slabs were optimized using VASP; this allows direct comparison of E_{surf} between calculations starting from a cleaved termination and those based on a USPEX-derived termination. The resulting slab always contained inversion centers, therefore are strictly nonpolar and the surface energy is well-defined. USPEX could not find the lowest energy termination in all cases, though we note that the surface terminations with low surface energy that USPEX could find can significantly depend on

the calculation settings and the initial structure population. For example, the lowest E_{surf} for the θ-Al_2O_3 ($11\bar{3}$) orientation obtained using USPEX in this study was more than 10 meV/Å^2 higher than a standard calculation from cleaved bulk. Therefore, taking the best result from two approaches, which are cleaved bulk calculations and GA calculations, is critical. The cleaved bulk was not explicitly included as an individual in USPEX calculations; however, atoms were randomly added to the cleaved bulk termination to generate the initial population. Separate USPEX calculations were conducted using the two cleaved bulk terminations, thus the termination discarded in step (a) is implicitly reflected in the GA steps. USPEX may find a termination with macroscopic facet orientations, which happened in the β-Ga_2O_3 ($60\bar{1}$) orientation [Fig. 3(b)], but this is an exception rather than the norm. There is no guarantee that the favorable facet widths are commensurate with a small in-plane area. The effect of edge energies will become more profound in microscopic facets where the facet width is of nanometer order, hence the surface energy could differ much from the right hand side of Eq. 4. Finally, the energy library must be updated to reflect lowering of the E_{surf} based on GA calculations in some orientations [step (e)], and surfaces that stabilize by macroscopic facet formation are identified again [step (f)]. Although USPEX calculations may reduce E_{surf} in an orientation that is stable against facet formation, further reduction of E_{surf} by USPEX calculations in competing orientations could make the E_{surf} higher than facet formation involving the competing orientation.

The application of this workflow to β-Ga_2O_3 and θ-Al_2O_3 is discussed below. Points removed in step (a) are shown in empty circles in Fig. 1. The gray points (gray filled circles and gray double circles) are metastable against macroscopic facet formation in step (b). USPEX calculations find a lower termination in some cases, and the original termination is shown as a black double circle. The USPEX termination identified as metastable against macroscopic facet formation in step (f) is shown in a black circle. Stable surfaces are shown in pointed symbols and are either obtained from cleaved bulk (red and empty triangles or USPEX (blue squares).

The process up to this point gives a set of reasonable terminations with a relatively small amount of calculations. However, we may be missing other terminations. For example, the θ-Al_2O_3 (310) orientation has a surface energy of 74 meV/Å^2 after USPEX calculations but that of the β-Ga_2O_3 (310) orientation is very high at 119 meV/Å^2 without USPEX calculations. It is unnatural that the lowest known β-Ga_2O_3 (310) surface energy is 1.6 times that of θ-Al_2O_3, especially as the surface energies of β-Ga_2O_3 tend to be lower

than θ-Al_2O_3. One can run GA calculations for all considered terminations to identify the stable termination and E_{surf}, but this is costly and very inefficient. On the other hand, investigation of unreasonable surfaces and missing reasonable and interesting surfaces should be avoided if possible. As a compromise, another loop to find stable surfaces (loop 2) is initiated. Additional USPEX calculations were performed on carefully prioritized orientations. Orientations that can accommodate stable microscopic facet terminations could significantly lower E_{surf} compared to macroscopic facet formation.

Therefore, as step (g), USPEX calculations, which may be able to find microscopic facet terminations, were additionally conducted for orientations with $\theta_1+\theta_2>70°$ and where the decrease in E_{surf} by macroscopic facet formation is less than 15 meV/Å^2. A large θ_1 and θ_2 results in a large increase in the surface area after facet formation [see Fig. 3(a)], therefore chances are higher that a smoother surface identified by USPEX has a E_{surf} smaller than the macroscopic facet. In θ-Al_2O_3, there are only two orientations below 7 meV/Å^2 and the rest is above 16 meV/Å^2, therefore 15 meV/Å^2 was adopted in consideration of this gap in the decrease of E_{surf}. There is a gap between 64° and 71° for $\theta_1+\theta_2$ in both β-Ga_2O_3 and θ-Al_2O_3, hence the cutoff was positioned in this gap. Orientations that were considered in this step are β-Ga_2O_3 (312), (11$\overline{1}$), (312), (51$\overline{2}$), (110), and (310) and θ-Al_2O_3 (51$\overline{2}$). USPEX calculations have been already calculated in step (c) for θ-Al_2O_3 (51$\overline{2}$) and has an E_{surf} higher than a competing surface, thus no additional calculation is necessary on this orientation that is known to be inaccessible.

The “Library” and “Facet” steps [(h) and (i), respectively] are subsequently performed after the additional USPEX calculations. Orientations where the additionally calculated USPEX termination is found to be stable against facet formation in step (i) are denoted in green diamonds and the original cleaved termination is shown as a gray double circle in Fig. 1. The β-Ga_2O_3 (111) orientation is stable against facet formation at step (f) but becomes unstable against facet formation in loop 2, therefore is shown as a black triangle. No additional stable surfaces of θ-Al_2O_3 were found in loop 2. All terminations considered “accessible”, which means that it is stable among other terminations in the same orientation and against macroscopic formation of facet pairs with different orientations, are shown in colored symbols in Fig. 1, and such terminations and surface energies for β-Ga_2O_3 and θ-Al_2O_3 are shown in Figs. 4 and 5, respectively.

In summary, orientations with accessible terminations are (100), (20$\overline{1}$), (310), (101), (11$\overline{2}$), (11$\overline{3}$), and (11$\overline{1}$) in β-Ga_2O_3 and (100), (20$\overline{1}$), (11$\overline{2}$), (310), (11$\overline{3}$), and (001)

in θ-Al_2O_3, respectively. The E_{surf} of the β-Ga_2O_3 ($11\bar{1}$) and θ-Al_2O_3 (001) orientations are 1.9 and 2.1 times that of the most stable (100) surface. Identifying these surfaces as accessible is very difficult without the proposed workflow.

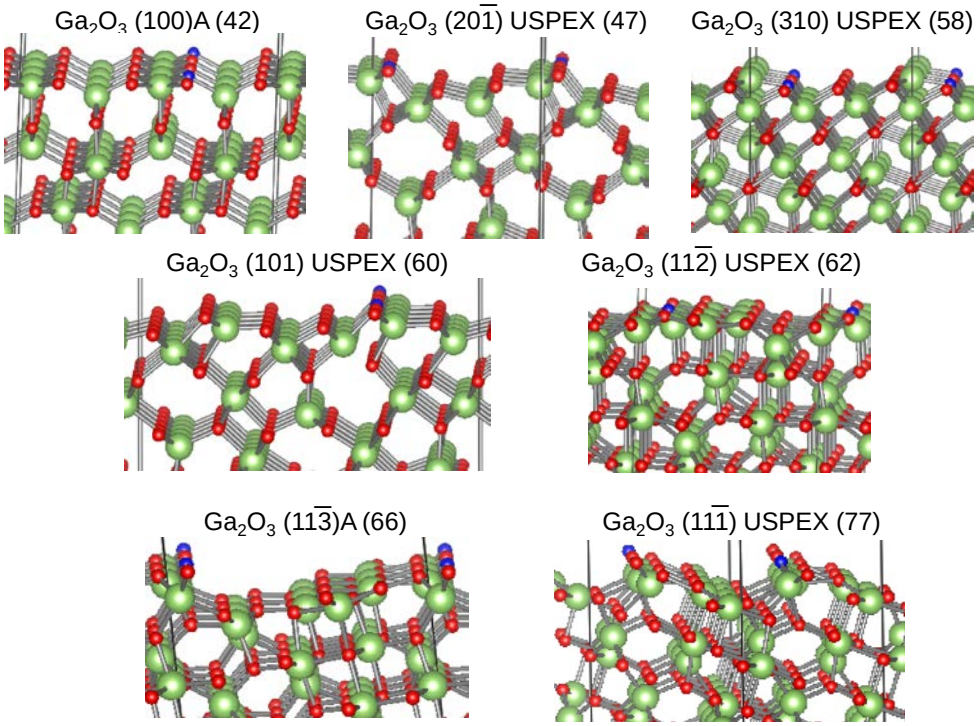

Fig. 4. Accessible terminations of β-Ga_2O_3. Green, red, and blue balls indicate Ga, O, and O with lowest E_{Ovac}, respectively. Numbers in brackets indicate the surface energy in meV/Å^2.

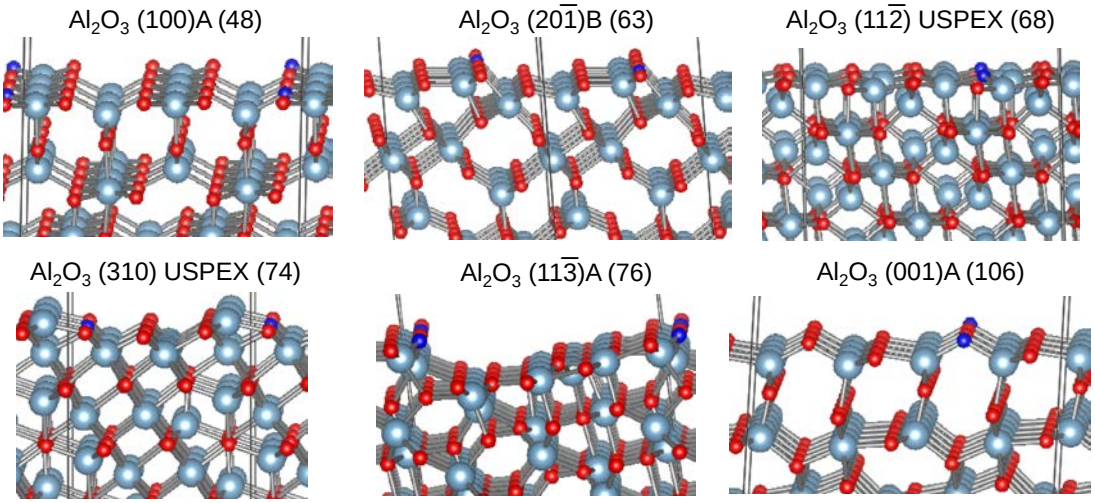

Fig. 5. Accessible terminations of θ-Al_2O_3. Light blue, red, and blue balls indicate Al, O, and O with lowest E_{Ovac}, respectively. Numbers in brackets indicate the surface energy in meV/Å^2.

3.2. E_{Ovac} and local coordination environment

Sites with low E_{Ovac} are desirable as reaction sites because of its high reactivity. The E_{Ovac} of the most stable surface, which is for the (100) orientation, is 4.36 and 6.57 eV in β-Ga_2O_3 and θ-Al_2O_3, respectively. These values are extremely high when we consider the minimum energy needed to remove neutral O from bulk, which is 4.07 and 6.36 eV, respectively. This may appear perplexing, but the reason is simple. The O site that can be removed with the lowest energy in bulk does not appear on the (100) surface.

Strategies to identify O sites with low E_{Ovac} are discussed below. The minimum E_{Ovac} in an accessible termination is 3.04 and 5.46 eV in the (101) and (20 $\overline{1}$) terminations for β-Ga_2O_3 and θ-Al_2O_3, respectively. The decrease in E_{Ovac} from the most stable surface is 1.32 and 1.11 eV for β-Ga_2O_3 and θ-Al_2O_3, respectively, indicating a large difference in reactivity between the terminations. The local coordination environment could strongly affect the E_{Ovac} in relatively stable terminations. There are two benefits if there is a good descriptor of E_{Ovac} related to the local coordination environment. First, the number of defect calculations could be reduced. Although defect calculations are much cheaper than GA calculations, the supercell used for defect calculations is larger than a standard slab model calculation and therefore takes much time. Second, it may be possible to design slight defects in accessible surfaces, such as step edges, to further lower E_{Ovac}. Surfaces with steps, which can be also considered models with facets, can be obtained with computational assistance using the algorithm in Ref. [116].

Lowering the coordination number does not necessarily reduce E_{Ovac}. For example, the E_{Ovac} of removal of a two-fold coordinated O from the β-Ga_2O_3 (11 $\overline{3}$)A termination is 3.12 eV [Fig. 6(a)]. The two Ga-O distances in Fig.6(a) are almost the same, and the Ga-O-Ga angle (109.7°) is very close to the bond angle in the ideal sp^3 coordination (109.5°). Therefore, the O is in a comfortable coordination environment although the coordination number is low. In contrast, the minimum E_{Ovac} for the β-Ga_2O_3 (101)USPEX termination is 3.04 eV [Fig. 6(b)], which is the smallest E_{Ovac} for an accessible termination. The O to be removed has two short and one long Ga-O bond. The distances of the short bonds are almost the same as in Fig. 6(a). However, the bond angle between these short bonds is

114.1°, which is right in the middle between the ideal sp^3 bond angle and the ideal sp^2 equatorial bond angle of 120°. The other two bond angles are also not close to either the ideal sp^2 axial bond angle of 90° nor the ideal sp^3 bond angle. This means that, although this O has three bonds instead of two, its unfavorable coordination environment decreases its stability. The former effect acts to increase E_{Ovac} compared to the O in Fig. 6(a), while the latter effect decreases E_{Ovac}.

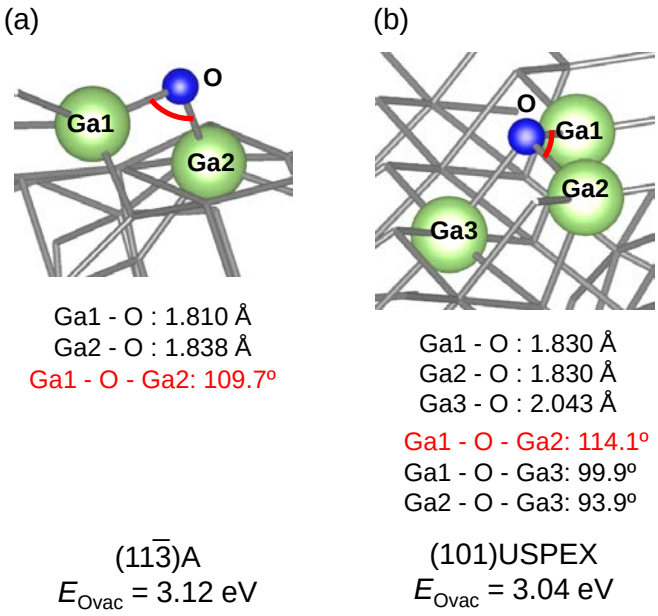

Fig. 6. Coordination environments of O with small E_{Ovac} in β-Ga_2O_3.

Based on the above observation, three geometrical descriptors for three-fold coordinated O are defined in Fig. 7. The vast majority of surface sites in accessible terminations in this study have three-fold coordination, thus we focus our analysis on such sites. The Ga plane is defined as the plane defined by the three Ga that bond to the O. Let Q be the circumcenter of the triangle where the vertices are the three Ga. The line perpendicular to the Ga plane that passes Q is defined as L. Let P be the point on line L that is closest to the O. All points on line L are equidistant to the three Ga, thus P can be considered as the position of O in an environment where the bond lengths are the same. The distance between P and a Ga is defined as the "ideal radius" *r*, and the distance between P and O as the "coordination distortion" *d*. The distance between P and Q is defined as the "trigonal pyramid height" *h*. Each of these descriptors depend on all bond lengths and bond angles, therefore provides information of the whole coordination environment, in contrast to more conventional and simple descriptors such as the

minimum (b_{min}), maximum (b_{max}), mean (b_{ave}) bond lengths and the difference between the longest and shortest bond ($b_{diff}=b_{max}-b_{min}$). Relations between E_{Ovac} for surface O in Figs. 4 and 5 and nine descriptors are investigated below. The descriptors are the aforementioned r, d, h, b_{min}, b_{max}, b_{ave}, and b_{diff} as well as an electronic structure descriptor, which is the BG of the model after O removal (BG_{desorb}), and a surface stability descriptor, which is the E_{surf} prior to O removal. The E_{surf} is not the fitted value, but is derived from the energy of the slab used for calculation of E_{Ovac} and the energy from a bulk calculation.

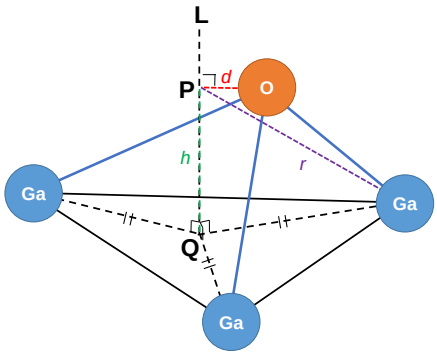

Fig. 7. Definition of coordination environment descriptors.

Figures 8 and 9 shows the surface O sites that are two- and three-fold coordinated for the accessible surfaces in Figs. 4 and 5, respectively. Two-fold coordinated surface O atoms (labeled as X) appear at the two highest E_{surf} surfaces only, and there the two-fold coordinated O have lowest E_{Ovac}. Tables 2 and 3 give the values of descriptors of O sites of Figs. 4 and 5. The atom ID in the tables correspond to those in the figures. Tables 4 and 5 gives R^2 for all combinations within E_{Ovac} and the descriptors for β-Ga_2O_3 and θ-Al_2O_3, respectively. By definition, the main diagonal values are unity and the tables are symmetric. First, we focus on R^2 between descriptors. The R^2 is very high at over 0.9 for the r-b_{ave} and d-b_{diff} pair. The former is a natural result because r is designed as the bond length when O is in an "ideal" position that is equidistant from the three O and still close to the actual position. Here, the bond lengths are evened out, thus should strongly reflect the average (mean) bond length b_{ave}. The R^2 between E_{Ovac} and a descriptor is considered next. The maximum R^2 for β-Ga_2O_3 and θ-Al_2O_3 is 0.54 and 0.64 with d and b_{min} respectively (Tables 2 and 3). E_{Ovac} is plotted against the descriptor in Fig. 10. A further increase in R^2 is attempted here by adding another descriptor. Plots of calculated E_{Ovac} against fitted E_{Ovac} from a linear combination with two descriptors are shown in Fig. 11. Note that increasing descriptors in the fit always increases R^2; the original R^2 can always

be recovered by setting the contribution of the added descriptor to zero. The R^2 improves to 0.73 and 0.82 for β-Ga_2O_3 and θ-Al_2O_3, respectively, and the additional descriptor is b_{ave} and d, respectively. The feature importance scores from nonlinear regression (random forest with 200 decision trees as implemented in scikit-learn[117] version 0.21.2) for E_{Ovac} are given in Fig. 12. There should be no highly dependent descriptors when calculating the feature importance, thus either r or b_{ave} and either d or b_{diff} must be eliminated. All four removal combinations yield very similar results, and the result that gives low RMSE and high R^2 among the combinations are shown as representatives. The R^2 is not impressive at 0.37 and 0.43 for β-Ga_2O_3 and θ-Al_2O_3, respectively, hence the results should be regarded as qualitative than quantitative. However, the feature importance results corroborate the results in Figs. 10 and 11; d is identified as the most important descriptor in β-Ga_2O_3, and b_{min} followed by $b_{max\text{-}min}$ (or d) have high feature importance in θ-Al_2O_3. Descriptors that reflect the total coordination environment, such as d, is more important in β-Ga_2O_3 while a descriptor of a very specific coordination environment, namely b_{min}, has strong influence on θ-Al_2O_3. One possible reason is the ionicity of the bonds. β-Ga_2O_3 is more covalent than θ-Al_2O_3, which can be inferred from the electronegativities of Ga and Al (1.8 and 1.6, respectively) and the Bader charge of O (1.2 and 1.7 in β-Ga_2O_3 and θ-Al_2O_3, respectively; the Bader charge of O is defined here as the electron density integrated over the Bader volume minus the number of electrons of an O atom). The overlap integral between orbitals becomes more important in covalent bonds, hence d, which reflects information on bond angles, has a stronger influence on E_{Ovac} in β-Ga_2O_3 than θ-Al_2O_3. The minimum bond length, which is considered most important in θ-Al_2O_3 based on our analysis, is somewhat important too in β-Ga_2O_3; the R^2 of b_{min} is 0.46, which is not very different from 0.52 for d. Therefore, the difference in ionicity might have changed the order of importance in two descriptors highly relevant in both materials. The minimum bond length should carry more importance than the maximum bond length because, due to anharmonicity of the interatomic potential, shortening of the bond length from the equilibrium bond length generally incurs a higher energy penalty compared to elongation by the same amount. This could be the reason why b_{min} is more important than b_{max} in both β-Ga_2O_3 than θ-Al_2O_3. Note that anharmonicity is found in major interatomic potential models, such as the Lennard-Jones and Morse potentials, and a direct consequence is positive thermal expansion that is observed in almost all materials. As a final note, we calculated E_{Ovac} of θ-Al_2O_3 for sites shown in Fig. 9 using a hybrid functional, namely HSE06. The HSE06 E_{Ovac} was consistently larger by 0.18±0.05eV compared to PBEsol with the exception of site 1 in $(20\,\bar{1})$ where HSE06 was larger by 0.01 eV, hence there are no significant changes to the trends. Although

hybrid functionals give more accurate band gaps compared to semi-local functionals, use of functionals with semi-local treatment of exchange-correlation is sufficient in this type of study.

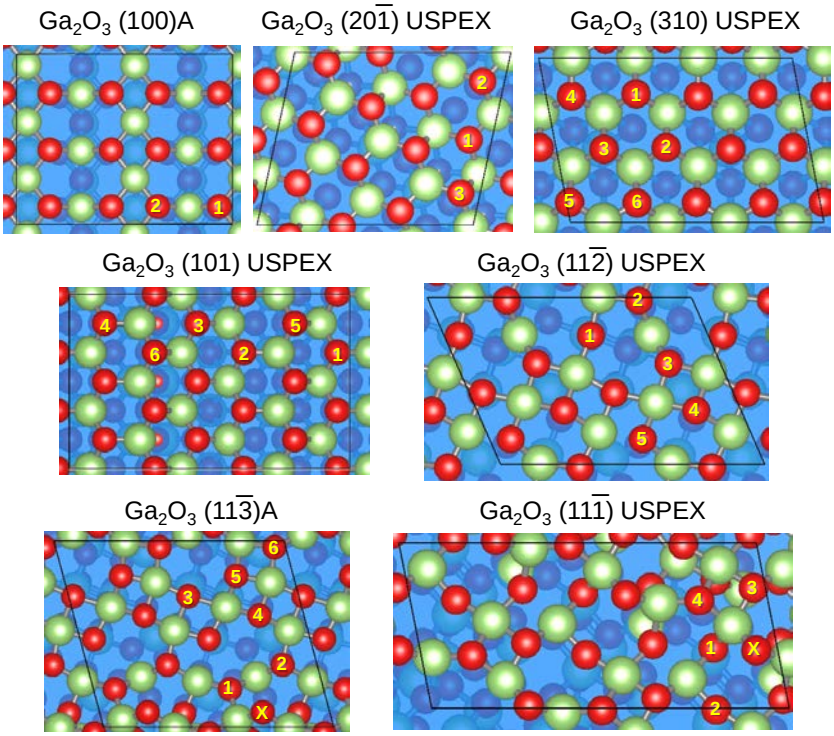

Fig. 8. Two- and three-fold coordinated surface sites of accessible terminations of β-Ga_2O_3, which are labeled with an X and a number, respectively. Green and red balls indicate Ga and O, respectively.

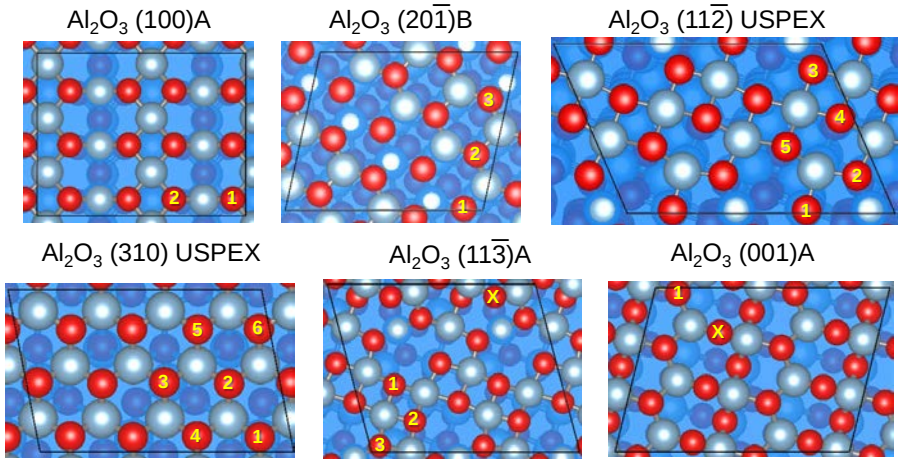

Fig. 9. Two- and three-fold coordinated surface sites of accessible terminations of θ-Al_2O_3, which are labeled with an X and a number, respectively. Blue and red balls indicate Al and O, respectively.

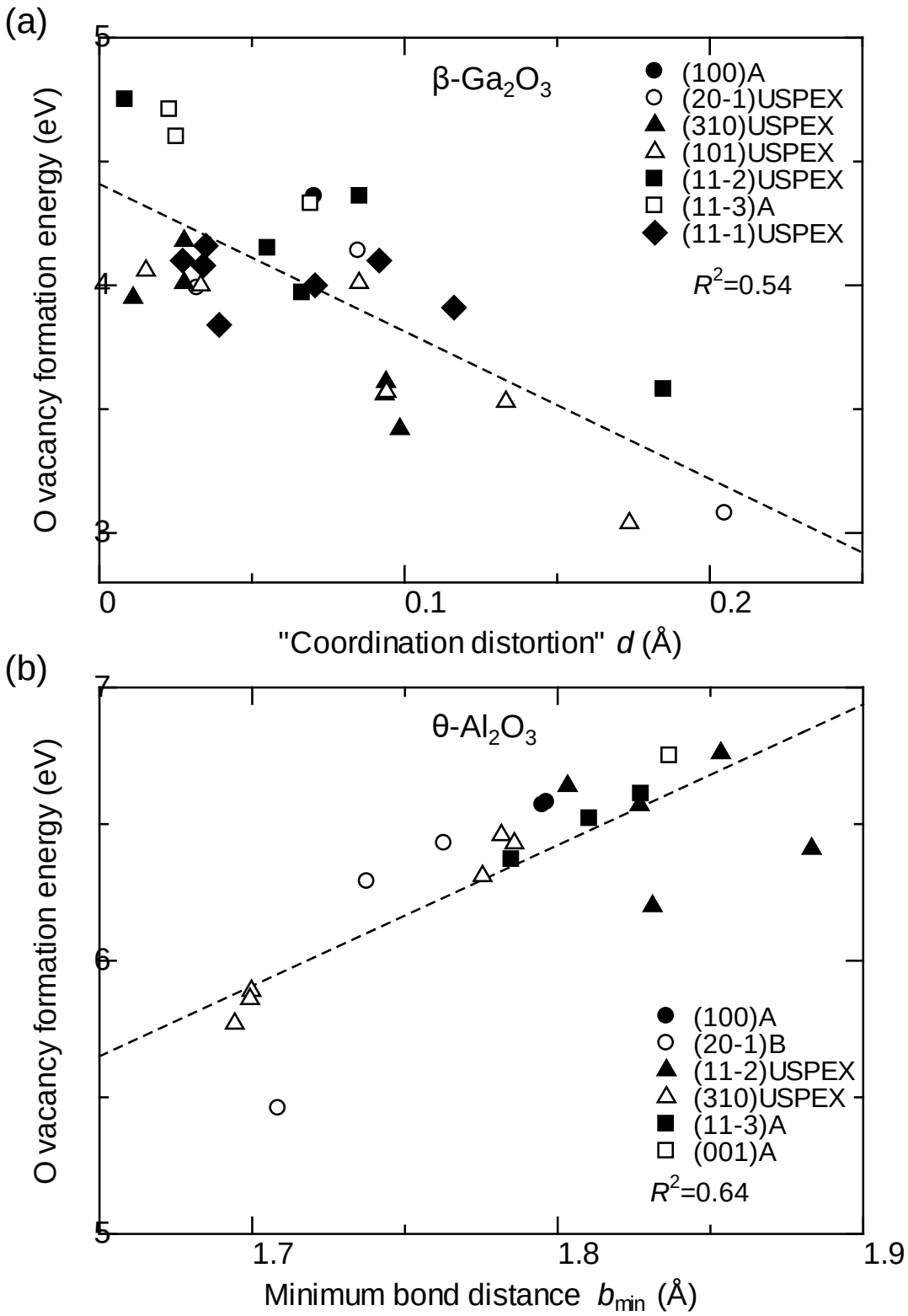

Fig. 10. E_{Ovac} vs one descriptor that maximizes R^2 for (a) β-Ga_2O_3 and (b) θ-Al_2O_3.

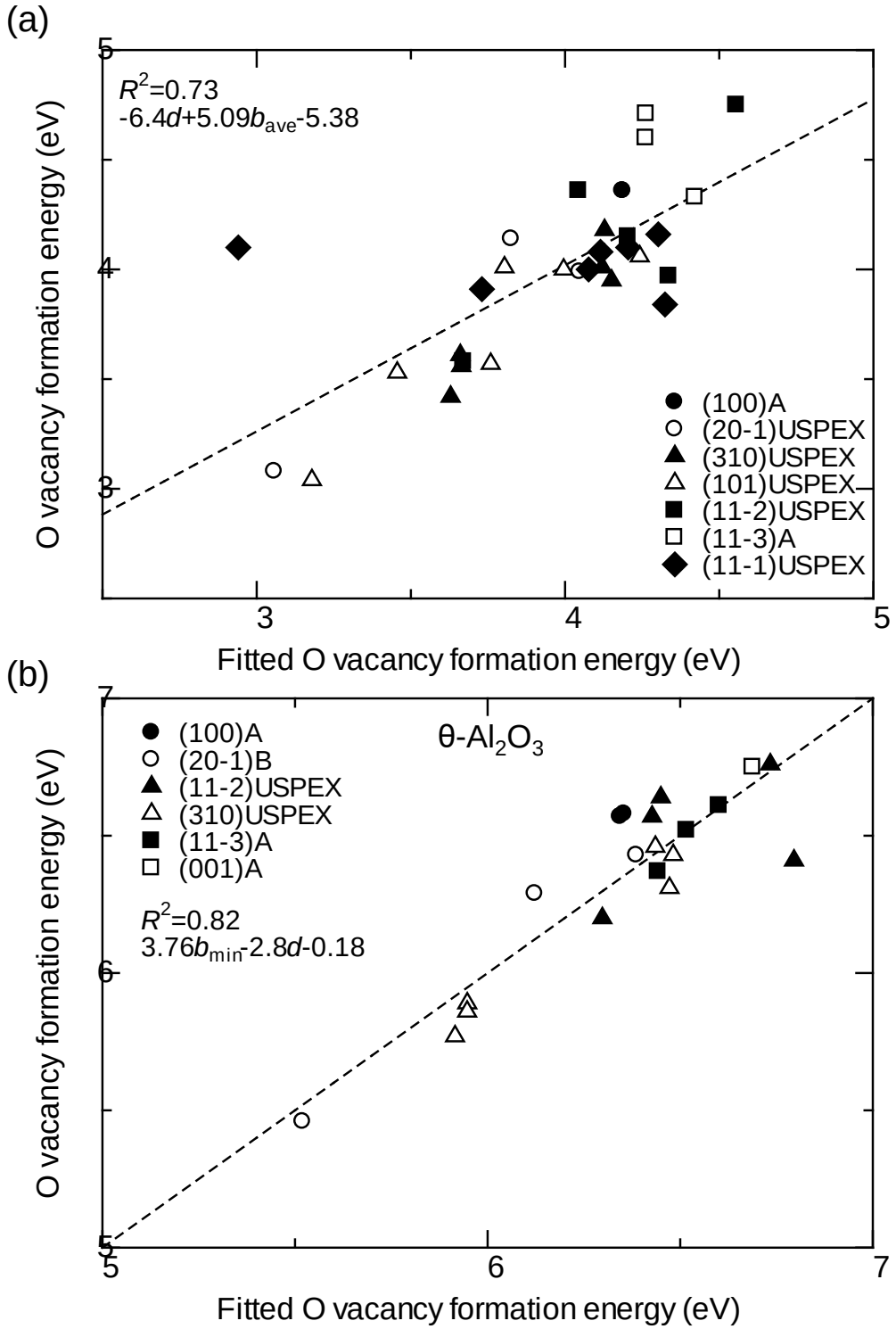

Fig. 11. Calculated E_{Ovac} vs fitted E_{Ovac} as a linear combination of two descriptors for (a) β-Ga_2O_3 and (b) θ-Al_2O_3.

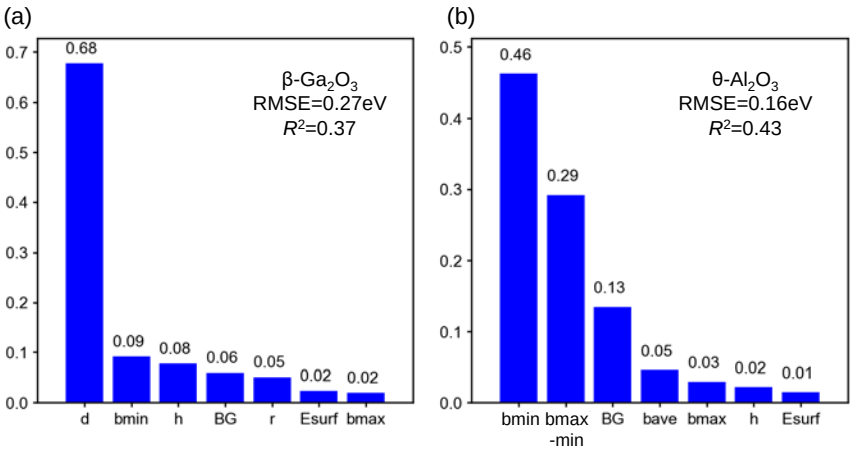

Fig. 12. Feature importance of descriptors for (a) β-Ga_2O_3 and (b) θ-Al_2O_3.

Table 2. Descriptors of three-fold coordinated surface O atoms for β-Ga_2O_3. Atom positions are shown in Fig. 8. Units of descriptors are eV for E_{Ovac} and BG_{desorb}, eV/Å^2 for E_{surf}, and Å for the rest.

Orientation	ID	E_{Ovac}	r	d	h	b_{min}	b_{ave}	b_{max}	b_{diff}	BG_{desorb}	E_{surf}
(100)	1	4.36	1.96	0.07	0.52	1.90	1.97	2.00	0.11	0.81	42
(100)	2	4.36	1.96	0.07	0.54	1.90	1.97	2.00	0.11	0.80	42
$(20\bar{1})$	1	4.14	1.91	0.08	0.69	1.84	1.92	1.96	0.12	1.13	54
$(20\bar{1})$	2	3.99	1.89	0.03	0.60	1.86	1.89	1.91	0.05	2.21	54
$(20\bar{1})$	3	3.08	1.90	0.20	0.86	1.83	1.92	2.08	0.25	2.16	54
(310)	1	4.18	1.90	0.03	0.87	1.88	1.90	1.92	0.04	0.91	50
(310)	2	3.95	1.89	0.01	0.85	1.88	1.89	1.89	0.02	1.41	50
(310)	3	4.01	1.90	0.03	0.90	1.88	1.90	1.92	0.04	1.39	50
(310)	4	3.42	1.89	0.10	0.56	1.80	1.89	1.95	0.16	1.47	50
(310)	5	3.61	1.89	0.09	0.56	1.80	1.89	1.95	0.15	1.54	50
(310)	6	3.56	1.89	0.09	0.60	1.80	1.89	1.95	0.15	1.78	50
(101)	1	3.57	1.91	0.09	0.70	1.83	1.91	1.96	0.13	1.03	65
(101)	2	4.01	1.91	0.09	0.62	1.83	1.91	1.95	0.12	0.43	65
(101)	3	4.06	1.91	0.02	0.81	1.90	1.91	1.92	0.02	0.09	65
(101)	4	4.00	1.88	0.03	0.57	1.85	1.88	1.90	0.05	1.48	65
(101)	5	3.53	1.90	0.13	0.84	1.85	1.90	2.02	0.17	1.02	65
(101)	6	3.04	1.89	0.17	0.85	1.83	1.90	2.04	0.21	1.58	65
$(11\bar{2})$	1	4.36	1.93	0.09	0.16	1.93	1.96	2.02	0.09	0.91	62
$(11\bar{2})$	2	4.75	1.96	0.01	0.50	1.96	1.96	1.97	0.01	1.25	62
$(11\bar{2})$	3	4.15	1.95	0.06	0.56	1.90	1.95	2.00	0.10	0.72	62
$(11\bar{2})$	4	3.97	2.01	0.07	0.43	1.94	1.99	2.03	0.09	0.63	62
$(11\bar{2})$	5	3.58	2.03	0.18	0.52	1.90	2.01	2.20	0.29	1.04	62
$(11\bar{3})$	1	4.71	1.92	0.02	0.29	1.91	1.92	1.95	0.04	1.66	66
$(11\bar{3})$	2	4.60	1.93	0.03	0.54	1.91	1.93	1.95	0.04	1.59	66
$(11\bar{3})$	3	4.33	2.01	0.07	1.02	1.98	2.01	2.07	0.09	0.62	66
$(11\bar{3})$	4	4.16	1.94	0.03	0.48	1.91	1.95	1.97	0.06	0.81	66
$(11\bar{3})$	5	4.10	1.91	0.03	0.42	1.90	1.92	1.94	0.04	0.83	66
$(11\bar{3})$	6	3.84	1.95	0.04	0.61	1.92	1.96	1.99	0.07	1.04	66
$(11\bar{1})$	1	4.00	1.95	0.07	0.05	1.91	1.95	2.01	0.11	0.93	70
$(11\bar{1})$	2	3.91	1.91	0.12	0.22	1.87	1.94	2.02	0.15	1.52	70
$(11\bar{1})$	3	4.08	1.91	0.03	0.51	1.87	1.91	1.94	0.06	1.01	70
$(11\bar{1})$	4	4.10	1.93	0.09	0.59	1.86	1.94	2.01	0.15	1.44	70

Table 3. Descriptors of three-fold coordinated surface O atoms for θ-Al_2O_3. Atom positions are shown in Fig. 9. Units of descriptors are eV for E_{Ovac} and BG_{desorb}, eV/Å^2 for E_{surf}, and Å for the rest.

Orientation	ID	E_{Ovac}	r	d	h	b_{min}	b_{ave}	b_{max}	b_{diff}	BG_{desorb}	E_{surf}
(100)	1	6.57	1.87	0.08	0.48	1.80	1.88	1.92	0.13	2.61	32
(100)	2	6.58	1.87	0.08	0.50	1.80	1.88	1.92	0.12	2.59	32
$(20\bar{1})$	1	6.29	1.82	0.08	0.62	1.74	1.82	1.86	0.12	2.72	50
$(20\bar{1})$	2	6.43	1.78	0.02	0.50	1.76	1.79	1.80	0.03	4.20	50
$(20\bar{1})$	3	5.46	1.79	0.26	0.78	1.71	1.82	2.03	0.32	3.74	50
$(11\bar{2})$	1	6.57	1.84	0.10	0.08	1.83	1.87	1.93	0.10	2.32	53
$(11\bar{2})$	2	6.76	1.87	0.02	0.45	1.85	1.87	1.89	0.03	2.68	53
$(11\bar{2})$	3	6.64	1.85	0.06	0.53	1.80	1.86	1.90	0.10	2.61	53
$(11\bar{2})$	4	6.41	1.92	0.04	0.37	1.88	1.91	1.94	0.05	1.99	53
$(11\bar{2})$	5	6.20	1.93	0.15	0.47	1.83	1.92	2.07	0.23	2.32	53
(310)	1	6.46	1.80	0.03	0.79	1.78	1.80	1.83	0.05	1.80	61
(310)	2	6.31	1.78	0.01	0.77	1.78	1.78	1.79	0.01	1.95	61
(310)	3	6.43	1.80	0.02	0.82	1.79	1.80	1.82	0.03	1.81	61
(310)	4	5.77	1.79	0.10	0.45	1.69	1.80	1.86	0.16	2.94	61
(310)	5	5.89	1.79	0.10	0.46	1.70	1.80	1.86	0.16	3.01	61
(310)	6	5.86	1.79	0.10	0.50	1.70	1.80	1.86	0.16	2.97	61
$(11\bar{3})$	1	6.52	1.85	0.04	0.41	1.81	1.85	1.88	0.07	2.26	66
$(11\bar{3})$	2	6.37	1.81	0.03	0.33	1.78	1.81	1.83	0.05	2.47	66
$(11\bar{3})$	3	6.61	1.86	0.03	0.57	1.83	1.86	1.89	0.06	2.72	66
(001)	1	6.75	1.84	0.01	0.33	1.84	1.84	1.86	0.02	2.68	91

Table 4. R^2 between E_{Ovac} and descriptors for the seven surfaces of β-Ga_2O_3.

	E_{Ovac}	r	d	h	b_{min}	b_{ave}	b_{max}	b_{diff}	BG_{desorb}	E_{surf}
E_{Ovac}	1	0.12	0.54	0.11	0.46	0.11	0.08	0.52	0.10	0.01
r	0.12	1	0.00	0.04	0.55	0.95	0.43	0.01	0.22	0.02
d	0.54	0.00	1	0.01	0.18	0.02	0.57	0.95	0.06	0.00
h	0.11	0.04	0.01	1	0.04	0.06	0.01	0.00	0.00	0.08
b_{min}	0.46	0.55	0.18	0.04	1	0.55	0.06	0.21	0.20	0.09
b_{ave}	0.11	0.95	0.02	0.06	0.55	1	0.52	0.03	0.20	0.03
b_{max}	0.08	0.43	0.57	0.01	0.06	0.52	1	0.58	0.01	0.03
b_{diff}	0.52	0.01	0.95	0.00	0.21	0.03	0.58	1	0.05	0.00
BG_{desorb}	0.10	0.22	0.06	0.00	0.20	0.20	0.01	0.05	1	0.04
E_{surf}	0.01	0.02	0.00	0.08	0.09	0.03	0.03	0.00	0.04	1

Table 5. R^2 between E_{Ovac} and descriptors for the six surfaces of θ-Al_2O_3.

	E_{Ovac}	r	d	h	b_{min}	b_{ave}	b_{max}	b_{diff}	BG_{desorb}	E_{surf}
E_{Ovac}	1	0.23	0.55	0.08	0.64	0.20	0.05	0.57	0.17	0.00
r	0.23	1	0.00	0.14	0.61	0.96	0.39	0.00	0.11	0.06
d	0.55	0.00	1	0.01	0.21	0.01	0.56	0.96	0.17	0.12
h	0.08	0.14	0.01	1	0.12	0.19	0.03	0.01	0.00	0.01
b_{min}	0.64	0.61	0.21	0.12	1	0.57	0.05	0.25	0.24	0.00
b_{ave}	0.20	0.96	0.01	0.19	0.57	1	0.49	0.01	0.09	0.09
b_{max}	0.05	0.39	0.56	0.03	0.05	0.49	1	0.55	0.01	0.12
b_{diff}	0.57	0.00	0.96	0.01	0.25	0.01	0.55	1	0.16	0.12
BG_{desorb}	0.17	0.11	0.17	0.00	0.24	0.09	0.01	0.16	1	0.02
E_{surf}	0.00	0.06	0.12	0.01	0.00	0.09	0.12	0.12	0.02	1

4. Conclusions

This paper investigated 34 orientations of β-Ga_2O_3 and θ-Al_2O_3 and developed a workflow to find surfaces that are regarded to be experimentally accessible. Surfaces that are metastable with respect to macroscopic facet formation are removed from consideration, and the termination of candidate orientations are investigated by calculating the E_{surf} of cleaved bulk and GA-suggested terminations. A total of seven and six accessible terminations were identified for β-Ga_2O_3 and θ-Al_2O_3, respectively. The lowest E_{Ovac}, which is a measure of reactivity of the O site, among the accessible terminations is 1.32 [(101) orientation] and 1.11 [$(20\bar{1})$ orientation] eV lower than the most stable termination, which is for the (100) orientation, in β-Ga_2O_3 and θ-Al_2O_3, respectively. Reduction in E_{Ovac} is possible by exposing unfavorable coordination environments at the surface, implying that formation of step and related local defects could further reduce E_{Ovac}. The E_{surf} of the highest accessible termination is roughly double of the lowest energy termination in both compounds, hence would be very difficult to consider without computational insight. We expect the proposed workflow would be of help to achieve emergence of new properties by efficiently exploring high E_{surf} yet accessible surfaces that have been overlooked.

Supporting Information.
Detailed data of cleaved slabs and details on USPEX calculations as well as the procedure of making a nonpolar slab with a USPEX-determined termination are supplied as Supporting Information.

Acknowledgments

This study was funded by the “Materials research by Information Integration” Initiative (MI^2I) project of the Support Program for Starting Up Innovation Hub as well as a grant (No. JPMJCR17J3) from CREST of the Japan Science and Technology Agency (JST), and by a Kakenhi Grant-in-Aid (No. 18K04692) from the Japan Society for the Promotion of Science (JSPS). Computing resources of the Research Institute for Information Technology at Kyushu University, ACCMS at Kyoto University, and the Supercomputer Center in the Institute for Solid State Physics at the University of Tokyo were used. The VESTA code [118] was used to draw Figs. 3-6, 8, 9, and S1-S10.

References

1. Ruiz Puigdollers, A.; Tosoni, S.; Pacchioni, G., Turning a Nonreducible into a Reducible Oxide Via Nanostructuring: Opposite Behavior of Bulk ZrO_2 and ZrO_2 Nanoparticles toward H_2 Adsorption. *J. Phys. Chem. C* **2016**, *120*, 15329-15337.

2. Tosoni, S.; Chen, H.-Y. T.; Pacchioni, G., A DFT Study of the Reactivity of Anatase TiO_2 and Tetragonal ZrO_2 Stepped Surfaces Compared to the Regular (101) Terraces. *ChemPhysChem* **2015**, *16*, 3642-3651.

3. Dulub, O.; Diebold, U.; Kresse, G., Novel Stabilization Mechanism on Polar Surfaces: Zno(0001)-Zn. *Phys. Rev. Lett.* **2003**, *90*, 016102.

4. Kresse, G.; Dulub, O.; Diebold, U., Competing Stabilization Mechanism for the Polar Zno(0001)-Zn Surface. *Phys. Rev. B* **2003**, *68*, 245409.

5. Staemmler, V.; Fink, K.; Meyer, B.; Marx, D.; Kunat, M.; Gil Girol, S.; Burghaus, U.; Wöll, C., Stabilization of Polar Zno Surfaces: Validating Microscopic Models by Using Co as a Probe Molecule. *Phys. Rev. Lett.* **2003**, *90*, 106102.

6. Wöll, C., The Chemistry and Physics of Zinc Oxide Surfaces. *Prog. Surf. Sci.* **2007**, *82*, 55-120.

7. Mora-Fonz, D.; Lazauskas, T.; Farrow, M. R.; Catlow, C. R. A.; Woodley, S. M.; Sokol, A. A., Why Are Polar Surfaces of ZnO Stable? *Chem. Mater.* **2017**, *29*, 5306-5320.

8. Blanck, D.; Berrier, E.; Paul, J.-F., First-Principles Investigation of the Relevant Surfaces Exposed by Polycrystalline $LaFeO_3$. *ChemCatChem* **2017**, *9*, 2383-2389.

9. Noguera, C., Polar Oxide Surfaces. *J. Phys.: Condens. Matter* **2000**, *12*, R367.

10. Goniakowski, J.; Finocchi, F.; Noguera, C., Polarity of Oxide Surfaces and Nanostructures. *Rep. Prog. Phys.* **2008**, *71*, 016501.

11. Ganduglia-Pirovano, M. V.; Hofmann, A.; Sauer, J., Oxygen Vacancies in Transition Metal and Rare Earth Oxides: Current State of Understanding and Remaining Challenges. *Surf. Sci. Rep.* **2007**, *62*, 219-270.

12. Oba, F.; Choi, M.; Togo, A.; Tanaka, I., Point Defects in ZnO: An Approach from First Principles. *Sci. Technol. Adv. Mater.* **2011**, *12*, 034302-034302.

13. Pacchioni, G., Oxygen Vacancy: The Invisible Agent on Oxide Surfaces. *ChemPhysChem* **2003**, *4*, 1041-1047.

14. Freysoldt, C.; Grabowski, B.; Hickel, T.; Neugebauer, J.; Kresse, G.; Janotti, A.; Van De Walle, C. G., First-Principles Calculations for Point Defects in Solids. *Rev. Mod. Phys.* **2014**, *86*, 253-305.

15. Emery, A. A.; Saal, J. E.; Kirklin, S.; Hegde, V. I.; Wolverton, C., High-Throughput Computational Screening of Perovskites for Thermochemical Water Splitting Applications. *Chem.*

Mater. **2016**, *28*, 5621-5634.

16. Petousis, I.; Mrdjenovich, D.; Ballouz, E.; Liu, M.; Winston, D.; Chen, W.; Graf, T.; Schladt, T. D.; Persson, K. A.; Prinz, F. B., High-Throughput Screening of Inorganic Compounds for the Discovery of Novel Dielectric and Optical Materials. *Scientific Data* **2017**, *4*, 160134.

17. Linderälv, C.; Lindman, A.; Erhart, P., A Unifying Perspective on Oxygen Vacancies in Wide Band Gap Oxides. *J. Phys. Chem. Lett.* **2018**, *9*, 222-228.

18. Jiang, W.; Zou, X.; Du, H.; Gan, L.; Xu, C.; Kang, F.; Duan, W.; Li, J., Universal Descriptor for Large-Scale Screening of High-Performance Mxene-Based Materials for Energy Storage and Conversion. *Chem. Mater.* **2018**, *30*, 2687-2693.

19. Fu, B.; Jia, Z.; Mu, W.; Yin, Y.; Zhang, J.; Tao, X., A Review of B-Ga2o3 Single Crystal Defects, Their Effects on Device Performance and Their Formation Mechanism. *Journal of Semiconductors* **2019**, *40*, 011804.

20. Jia, J.; Qian, C.; Dong, Y.; Li, Y. F.; Wang, H.; Ghoussoub, M.; Butler, K. T.; Walsh, A.; Ozin, G. A., Heterogeneous Catalytic Hydrogenation of CO_2 by Metal Oxides: Defect Engineering – Perfecting Imperfection. *Chem. Soc. Rev.* **2017**, *46*, 4631-4644.

21. Puigdollers, A. R.; Schlexer, P.; Tosoni, S.; Pacchioni, G., Increasing Oxide Reducibility: The Role of Metal/Oxide Interfaces in the Formation of Oxygen Vacancies. *ACS Catalysis* **2017**, *7*, 6493-6513.

22. Zhu, Y.; Liu, X.; Jin, S.; Chen, H.; Lee, W.; Liu, M.; Chen, Y., Anionic Defect Engineering of Transition Metal Oxides for Oxygen Reduction and Evolution Reactions. *Journal of Materials Chemistry A* **2019**, *7*, 5875-5897.

23. Mars, P.; van Krevelen, D. W., Oxidations Carried out by Means of Vanadium Oxide Catalysts. *Chem. Eng. Sci.* **1954**, *3*, 41-59.

24. Chen, K.; Khodakov, A.; Yang, J.; Bell, A. T.; Iglesia, E., Isotopic Tracer and Kinetic Studies of Oxidative Dehydrogenation Pathways on Vanadium Oxide Catalysts. *J. Catal.* **1999**, *186*, 325-333.

25. Doornkamp, C.; Ponec, V., The Universal Character of the Mars and Van Krevelen Mechanism. *J. Mol. Catal. A: Chem.* **2000**, *162*, 19-32.

26. Widmann, D.; Behm, R. J., Activation of Molecular Oxygen and the Nature of the Active Oxygen Species for Co Oxidation on Oxide Supported Au Catalysts. *Acc. Chem. Res.* **2014**, *47*, 740-749.

27. Kumar, G.; Lau, S. L. J.; Krcha, M. D.; Janik, M. J., Correlation of Methane Activation and Oxide Catalyst Reducibility and Its Implications for Oxidative Coupling. *ACS Catalysis* **2016**, *6*, 1812-1821.

28. Hinuma, Y.; Toyao, T.; Kamachi, T.; Maeno, Z.; Takakusagi, S.; Furukawa, S.; Takigawa, I.; Shimizu, K.-i., Density Functional Theory Calculations of Oxygen Vacancy Formation and

Subsequent Molecular Adsorption on Oxide Surfaces. *J. Phys. Chem. C* **2018**, *122*, 29435-29444.

29. Agarwal, S.; Zhu, X.; Hensen, E. J. M.; Lefferts, L.; Mojet, B. L., Defect Chemistry of Ceria Nanorods. *Journal of Physical Chemistry C* **2014**, *118*, 4131-4142.

30. Werner, K., et al., Toward an Understanding of Selective Alkyne Hydrogenation on Ceria: On the Impact of O Vacancies on H_2 interaction with CeO_2 (111). *J. Am. Chem. Soc.* **2017**, *139*, 17608-17616.

31. Yang, C.; Yu, X.; Heißler, S.; Weidler, P. G.; Nefedov, A.; Wang, Y.; Wöll, C.; Kropp, T.; Paier, J.; Sauer, J., O_2 activation on Ceria Catalysts—the Importance of Substrate Crystallographic Orientation. *Angewandte Chemie - International Edition* **2017**, *56*, 16399-16404.

32. Zhang, Z.; Bondarchuk, O.; White, J. M.; Kay, B. D.; Dohnálek, Z., Imaging Adsorbate O-H Bond Cleavage: Methanol on TiO2(110). *J. Am. Chem. Soc.* **2006**, *128*, 4198-4199.

33. Pacchioni, G.; Freund, H., Electron Transfer at Oxide Surfaces. The Mgo Paradigm: From Defects to Ultrathin Films. 2013; Vol. 113, pp 4035-4072.

34. Setvín, M.; Wagner, M.; Schmid, M.; Parkinson, G. S.; Diebold, U., Surface Point Defects on Bulk Oxides: Atomically-Resolved Scanning Probe Microscopy. *Chem. Soc. Rev.* **2017**, *46*, 1772-1784.

35. Tong, X.; Benz, L.; Chrétien, S.; Metiu, H.; Bowers, M. T.; Buratto, S. K., Direct Visualization of Water-Induced Relocation of Au Atoms from Oxygen Vacancies on a TiO_2(110) Surface. *Journal of Physical Chemistry C* **2010**, *114*, 3987-3990.

36. Honkala, K., Tailoring Oxide Properties: An Impact on Adsorption Characteristics of Molecules and Metals. *Surf. Sci. Rep.* **2014**, *69*, 366-388.

37. Albuquerque, A. R.; Bruix, A.; Dos Santos, I. M. G.; Sambrano, J. R.; Illas, F., Dft Study on Ce-Doped Anatase TiO_2: Nature of Ce^{3+} and Ti^{3+} Centers Triggered by Oxygen Vacancy Formation. *Journal of Physical Chemistry C* **2014**, *118*, 9677-9689.

38. Haubrich, J.; Kaxiras, E.; Friend, C. M., The Role of Surface and Subsurface Point Defects for Chemical Model Studies on TiO_2: A First-Principles Theoretical Study of Formaldehyde Bonding on Rutile TiO_2 (110). *Chemistry - A European Journal* **2011**, *17*, 4496-4506.

39. Gerosa, M.; Bottani, C. E.; Caramella, L.; Onida, G.; Di Valentin, C.; Pacchioni, G., Defect Calculations in Semiconductors through a Dielectric-Dependent Hybrid Dft Functional: The Case of Oxygen Vacancies in Metal Oxides. *J. Chem. Phys.* **2015**, *143*, 134702-134702.

40. Dickens, C. F.; Nørskov, J. K., A Theoretical Investigation into the Role of Surface Defects for Oxygen Evolution on RuO_2. *J. Phys. Chem. C* **2017**, *121*, 18516-18524.

41. Rellán-Piñeiro, M.; López, N., One Oxygen Vacancy, Two Charge States: Characterization of Reduced A-MoO_3 (010) through Theoretical Methods. *The Journal of Physical Chemistry Letters* **2018**, *9*, 2568-2573.

42. Santen, R. A. v.; Neurock, M.; Shetty, S. G., Reactivity Theory of Transition-Metal Surfaces: A Brønsted−Evans−Polanyi Linear Activation Energy−Free-Energy Analysis. *Chem. Rev.* **2010**, *110*, 2005-2048.

43. Medford, A. J.; Vojvodic, A.; Hummelshøj, J. S.; Voss, J.; Abild-Pedersen, F.; Studt, F.; Bligaard, T.; Nilsson, A.; Nørskov, J. K., From the Sabatier Principle to a Predictive Theory of Transition-Metal Heterogeneous Catalysis. *J. Catal.* **2015**, *328*, 36-42.

44. Deml, A. M.; Stevanović, V.; Muhich, C. L.; Musgrave, C. B.; O'Hayre, R., Oxide Enthalpy of Formation and Band Gap Energy as Accurate Descriptors of Oxygen Vacancy Formation Energetics. *Energy Environ. Sci.* **2014**, *7*, 1996-2004.

45. Galazka, Z., B-Ga2o3 for Wide-Bandgap Electronics and Optoelectronics. *Semicond. Sci. Technol.* **2018**, *33*, 113001.

46. Pearton, S. J.; Yang, J.; Cary, P. H.; Ren, F.; Kim, J. H.; Tadjer, M. J.; Mastro, M. A., A Review of Ga_2O_3 Materials, Processing, and Devices. *Applied Physics Reviews* **2018**, *5*, 011301.

47. Oshima, T.; Okuno, T.; Arai, N.; Suzuki, N.; Ohira, S.; Fujita, S., Vertical Solar-Blind Deep-Ultraviolet Schottky Photodetectors Based on B-Ga_2O_3 substrates. *Appl. Phys. Express* **2008**, *1*, 011202.

48. Guo, D. Y.; Wu, Z. P.; An, Y. H.; Guo, X. C.; Chu, X. L.; Sun, C. L.; Li, L. H.; Li, P. G.; Tang, W. H., Oxygen Vacancy Tuned Ohmic-Schottky Conversion for Enhanced Performance in B-Ga_2O_3 Solar-Blind Ultraviolet Photodetectors. *Appl. Phys. Lett.* **2014**, *105*, 023507.

49. Fleischer, M.; Höllbauer, L.; Meixner, H., Effect of the Sensor Structure on the Stability of Ga2o3 Sensors for Reducing Gases. *Sens. Actuator B-Chem.* **1994**, *18*, 119-124.

50. Afzal, A., B-Ga_2O_3 Nanowires and Thin Films for Metal Oxide Semiconductor Gas Sensors: Sensing Mechanisms and Performance Enhancement Strategies. *Journal of Materiomics* **2019**, *5*, 542-557.

51. Ueda, N.; Hosono, H.; Waseda, R.; Kawazoe, H., Synthesis and Control of Conductivity of Ultraviolet Transmitting B-Ga_2O_3 Single Crystals. *Appl. Phys. Lett.* **1997**, *70*, 3561-3563.

52. Orita, M.; Ohta, H.; Hirano, M.; Hosono, H., Deep-Ultraviolet Transparent Conductive B-Ga2o3 Thin Films. *Appl. Phys. Lett.* **2000**, *77*, 4166-4168.

53. Higashiwaki, M.; Sasaki, K.; Murakami, H.; Kumagai, Y.; Koukitu, A.; Kuramata, A.; Masui, T.; Yamakoshi, S., Recent Progress in Ga_2O_3 Power Devices. *Semicond. Sci. Technol.* **2016**, *31*, 034001.

54. Mastro, M. A.; Kuramata, A.; Calkins, J.; Kim, J.; Ren, F.; Pearton, S. J., Perspective—Opportunities and Future Directions for Ga_2O_3. *ECS J. Solid State Sci. Technol.* **2017**, *6*, P356-P359.

55. Jin, S., et al., Effect of Phase Junction Structure on the Photocatalytic Performance in Overall Water Splitting: Ga_2O_3 Photocatalyst as an Example. *J. Phys. Chem. C* **2015**, *119*, 18221-

18228.

56. Qu, J.; Tsang, S. C. E.; Gong, X.-Q., A Dft Study on Surface Dependence of B-Ga_2O_3 for CO_2 Hydrogenation to CH_3OH. *J. Mol. Model.* **2014**, *20*, 2543.

57. Liu, T.; Feng, Z.; Li, Q.; Yang, J.; Li, C.; Dupuis, M., Role of Oxygen Vacancies on Oxygen Evolution Reaction Activity: B-Ga_2O_3 as a Case Study. *Chem. Mater.* **2018**, *30*, 7714-7726.

58. Busca, G., The Surface of Transitional Aluminas: A Critical Review. *Catal. Today* **2014**, *226*, 2-13.

59. Gangwar, J.; Gupta, B. K.; Tripathi, S. K.; Srivastava, A. K., Phase Dependent Thermal and Spectroscopic Responses of Al_2O_3 Nanostructures with Different Morphogenesis. *Nanoscale* **2015**, *7*, 13313-13344.

60. Moses-DeBusk, M.; Yoon, M.; Allard, L. F.; Mullins, D. R.; Wu, Z.; Yang, X.; Veith, G.; Stocks, G. M.; Narula, C. K., Co Oxidation on Supported Single Pt Atoms: Experimental and Ab Initio Density Functional Studies of Co Interaction with Pt Atom on Θ-Al_2O_3 (010) Surface. *J. Am. Chem. Soc.* **2013**, *135*, 12634-12645.

61. Peterson, E. J., et al., Low-Temperature Carbon Monoxide Oxidation Catalysed by Regenerable Atomically Dispersed Palladium on Alumina. *Nat. Commun.* **2014**, *5*, 4885.

62. Yang, T.; Fukuda, R.; Hosokawa, S.; Tanaka, T.; Sakaki, S.; Ehara, M., A Theoretical Investigation on Co Oxidation by Single-Atom Catalysts M1/Γ-Al_2O_3 (M=Pd, Fe, Co, and Ni). *ChemCatChem* **2017**, *9*, 1222-1229.

63. Narula, C. K.; Allard, L. F.; Stocks, G. M.; Moses-DeBusk, M., Remarkable No Oxidation on Single Supported Platinum Atoms. *Sci. Rep.* **2014**, *4*, 7238.

64. Dixit, M.; Kostetskyy, P.; Mpourmpakis, G., Structure–Activity Relationships in Alkane Dehydrogenation on Γ-Al_2O_3: Site-Dependent Reactions. *ACS Catalysis* **2018**, *8*, 11570-11578.

65. Hamberg, I.; Granqvist, C. G., Evaporated Sn-Doped In2o3 Films: Basic Optical Properties and Applications to Energy-Efficient Windows. *J. Appl. Phys.* **1986**, *60*, R123-R160.

66. Granqvist, C. G.; Hultåker, A., Transparent and Conducting Ito Films: New Developments and Applications. *Thin Solid Films* **2002**, *411*, 1-5.

67. Walsh, A., et al., Nature of the Band Gap of In_2O_3 Revealed by First-Principles Calculations and X-Ray Spectroscopy. *Phys. Rev. Lett.* **2008**, *100*, 167402.

68. Sanders, D.; Simon, U., High-Throughput Gas Sensing Screening of Surface-Doped In_2O_3. *J. Comb. Chem.* **2007**, *9*, 53-61.

69. Ye, J.; Liu, C.; Mei, D.; Ge, Q., Active Oxygen Vacancy Site for Methanol Synthesis from CO_2 Hydrogenation on In_2O_3 (110): A Dft Study. *ACS Catalysis* **2013**, *3*, 1296-1306.

70. Sun, K.; Fan, Z.; Ye, J.; Yan, J.; Ge, Q.; Li, Y.; He, W.; Yang, W.; Liu, C.-j., Hydrogenation of CO_2 to Methanol over In_2O_3 Catalyst. *Journal of CO_2 Utilization* **2015**, *12*, 1-

6.

71. Tsoukalou, A.; Abdala, P. M.; Stoian, D.; Huang, X.; Willinger, M.-G.; Fedorov, A.; Müller, C. R., Structural Evolution and Dynamics of an In_2O_3 Catalyst for CO_2 Hydrogenation to Methanol: An Operando XAS-XRD and in Situ Tem Study. *J. Am. Chem. Soc.* **2019**, *141*, 13497-13505.

72. Rui, N.; Wang, Z.; Sun, K.; Ye, J.; Ge, Q.; Liu, C.-j., CO_2 Hydrogenation to Methanol over Pd/In_2O_3: Effects of Pd and Oxygen Vacancy. *Applied Catalysis B: Environmental* **2017**, *218*, 488-497.

73. Frei, M. S.; Mondelli, C.; García-Muelas, R.; Kley, K. S.; Puértolas, B.; López, N.; Safonova, O. V.; Stewart, J. A.; Curulla Ferré, D.; Pérez-Ramírez, J., Atomic-Scale Engineering of Indium Oxide Promotion by Palladium for Methanol Production Via CO=Hydrogenation. *Nat. Commun.* **2019**, *10*, 3377.

74. Martin, O.; Martín, A. J.; Mondelli, C.; Mitchell, S.; Segawa, T. F.; Hauert, R.; Drouilly, C.; Curulla-Ferré, D.; Pérez-Ramírez, J., Indium Oxide as a Superior Catalyst for Methanol Synthesis by CO_2 Hydrogenation. *Angew. Chem. Int. Ed.* **2016**, *55*, 6261-6265.

75. Sorribes, I.; Lemos, S. C. S.; Martín, S.; Mayoral, A.; Lima, R. C.; Andrés, J., Palladium Doping of In_2O_3 Towards a General and Selective Catalytic Hydrogenation of Amides to Amines and Alcohols. *Catalysis Science & Technology* **2019**, *9*, 6965-6976.

76. Hinuma, Y.; Gake, T.; Oba, F., Band Alignment at Surfaces and Heterointerfaces of Al_2O_3, Ga_2O_3, In_2O_3, and Related Group-III Oxide Polymorphs: A First-Principles Study. *Phys. Rev. Mater.* **2019**, *3*, 084605.

77. Blöchl, P. E., Projector Augmented-Wave Method. *Phys. Rev. B* **1994**, *50*, 17953-17979.

78. Kresse, G.; Furthmüller, J., Efficient Iterative Schemes for Ab Initio Total-Energy Calculations Using a Plane-Wave Basis Set. *Phys. Rev. B* **1996**, *54*, 11169-11186.

79. Kresse, G.; Joubert, D., From Ultrasoft Pseudopotentials to the Projector Augmented-Wave Method. *Phys. Rev. B* **1999**, *59*, 1758-1775.

80. Perdew, J. P.; Ruzsinszky, A.; Csonka, G. I.; Vydrov, O. A.; Scuseria, G. E.; Constantin, L. A.; Zhou, X.; Burke, K., Restoring the Density-Gradient Expansion for Exchange in Solids and Surfaces. *Phys. Rev. Lett.* **2008**, *100*, 136406.

81. Perdew, J. P.; Burke, K.; Ernzerhof, M., Generalized Gradient Approximation Made Simple. *Phys. Rev. Lett.* **1996**, *77*, 3865-3868.

82. Hinuma, Y.; Hayashi, H.; Kumagai, Y.; Tanaka, I.; Oba, F., Comparison of Approximations in Density Functional Theory Calculations: Energetics and Structure of Binary Oxides. *Phys. Rev. B* **2017**, *96*, 094102.

83. Sun, J.; Ruzsinszky, A.; Perdew, J. P., Strongly Constrained and Appropriately Normed Semilocal Density Functional. *Phys. Rev. Lett.* **2015**, *115*, 036402.

84. Heyd, J.; Scuseria, G.; Ernzerhof, M., Hybrid Functionals Based on a Screened Coulomb Potential. *J. Chem. Phys.* **2003**, *118*, 8207.

85. Heyd, J.; Scuseria, G. E.; Ernzerhof, M., Erratum: “Hybrid Functionals Based on a Screened Coulomb Potential” [J. Chem. Phys. 118, 8207 (2003)]. *J. Chem. Phys.* **2006**, *124*, 219906.

86. Krukau, A. V.; Vydrov, O. A.; Izmaylov, A. F.; Scuseria, G. E., Influence of the Exchange Screening Parameter on the Performance of Screened Hybrid Functionals. *J. Chem. Phys.* **2006**, *125*, 224106-5.

87. Rebien, M.; Henrion, W.; Hong, M.; Mannaerts, J. P.; Fleischer, M., Optical Properties of Gallium Oxide Thin Films. *Appl. Phys. Lett.* **2002**, *81*, 250-252.

88. Orita, M.; Ohta, H.; Hirano, M., Deep-Ultraviolet Transparent Conductive B-Ga_2O_3 Thin Films. *Appl. Phys. Lett.* **2000**, *77*, 4166-4168.

89. Franchy, R.; Schmitz, G.; Gassmann, P.; Bartolucci, F., Growth of Thin, Crystalline Oxide, Nitride, and Oxynitride Films on Nial and Coga Surfaces. *Appl. Phys. A* **1997**, *65*, 551-566.

90. Tasker, P. W., The Stability of Ionic Crystal Surfaces. *J. Phys. C: Solid State Phys.* **1979**, *12*, 4977.

91. Hinuma, Y.; Kumagai, Y.; Oba, F.; Tanaka, I., Categorization of Surface Polarity from a Crystallographic Approach. *Comp. Mater. Sci.* **2016**, *113*, 221-230.

92. Hinuma, Y.; Oba, F.; Kumagai, Y.; Tanaka, I., Ionization Potentials of (112) and (11-2) Facet Surfaces of $CuInSe_2$ and $CuGaSe_2$. *Phys. Rev. B* **2012**, *86*, 245433.

93. Deml, A. M.; Holder, A. M.; O’Hayre, R. P.; Musgrave, C. B.; Stevanović, V., Intrinsic Material Properties Dictating Oxygen Vacancy Formation Energetics in Metal Oxides. *The Journal of Physical Chemistry Letters* **2015**, *6*, 1948-1953.

94. Hinuma, Y.; Kamachi, T.; Hamamoto, N., Automated Identification of Facet Pair Orientations . *Mater. Trans*, **2020**, *accepted*. https://doi.org/10.2320/matertrans.MT-MN2019004

95. Oganov, A. R.; Ono, S., Theoretical and Experimental Evidence for a Post-Perovskite Phase of $MgSiO_3$ in Earth's D″ Layer. *Nature* **2004**, *430*, 445-448.

96. Oganov, A. R.; Glass, C. W., Crystal Structure Prediction Using Ab Initio Evolutionary Techniques: Principles and Applications. *J. Chem. Phys.* **2006**, *124*, 244704.

97. Oganov, A. R.; Lyakhov, A. O.; Valle, M., How Evolutionary Crystal Structure Prediction Works—and Why. *Acc. Chem. Res.* **2011**, *44*, 227-237.

98. Zhu, Q.; Li, L.; Oganov, A. R.; Allen, P. B., Evolutionary Method for Predicting Surface Reconstructions with Variable Stoichiometry. *Phys. Rev. B* **2013**, *87*, 195317.

99. Abraham, N. L.; Probert, M. I. J., A Periodic Genetic Algorithm with Real-Space

Representation for Crystal Structure and Polymorph Prediction. *Phys. Rev. B* **2006**, *73*, 224104.
100. Wang, Y.; Lv, J.; Zhu, L.; Ma, Y., Crystal Structure Prediction Via Particle-Swarm Optimization. *Phys. Rev. B* **2010**, *82*, 094116.
101. Wang, Y.; Lv, J.; Zhu, L.; Ma, Y., Calypso: A Method for Crystal Structure Prediction. *Comput. Phys. Commun.* **2012**, *183*, 2063-2070.
102. Le, T. C.; Winkler, D. A., Discovery and Optimization of Materials Using Evolutionary Approaches. *Chem. Rev.* **2016**, *116*, 6107-6132.
103. Lee, I.-H.; Oh, Y. J.; Kim, S.; Lee, J.; Chang, K. J., Ab Initio Materials Design Using Conformational Space Annealing and Its Application to Searching for Direct Band Gap Silicon Crystals. *Comput. Phys. Commun.* **2016**, *203*, 110-121.
104. Yamashita, T.; Sato, N.; Kino, H.; Miyake, T.; Tsuda, K.; Oguchi, T., Crystal Structure Prediction Accelerated by Bayesian Optimization. *Phys. Rev. Mater.* **2018**, *2*, 013803.
105. Takasao, G.; Wada, T.; Thakur, A.; Chammingkwan, P.; Terano, M.; Taniike, T., Machine Learning-Aided Structure Determination for $TiCl_4$–Capped $MgCl_2$ Nanoplate of Heterogeneous Ziegler–Natta Catalyst. *ACS Catalysis* **2019**, *9*, 2599-2609.
106. Avery, P.; Toher, C.; Curtarolo, S.; Zurek, E., Xtalopt version R12: An Open-Source Evolutionary Algorithm for Crystal Structure Prediction. *Comput. Phys. Commun.* **2019**, *237*, 274-275.
107. Ishikawa, T.; Miyake, T.; Shimizu, K., Materials Informatics Based on Evolutionary Algorithms: Application to Search for Superconducting Hydrogen Compounds. *Phys. Rev. B* **2019**, *100*, 174506.
108. Ganguly Neogi, S.; Chaudhury, P., Structural, Spectroscopic Aspects, and Electronic Properties of (TiO_2)N Clusters: A Study Based on the Use of Natural Algorithms in Association with Quantum Chemical Methods. *J. Comput. Chem.* **2014**, *35*, 51-61.
109. Neogi, S. G.; Chaudhury, P., Structure, Spectroscopy and Electronic Properties of Neutral Lattice-Like (MgO)Nclusters: A Study Based on a Blending of Dft with Stochastic Algorithms Inspired by Natural Processes. *Struct. Chem.* **2014**, *25*, 1229-1244.
110. Zakaryan, H. A.; Kvashnin, A. G.; Oganov, A. R., Stable Reconstruction of the (110) Surface and Its Role in Pseudocapacitance of Rutile-Like RuO_2. *Sci. Rep.* **2017**, *7*, 10357.
111. Feya, O. D.; Wang, Q.; Lepeshkin, S. V.; Baturin, V. S.; Uspenskii, Y. A.; Oganov, A. R., Tetrahedral Honeycomb Surface Reconstructions of Quartz, Cristobalite and Stishovite. *Sci. Rep.* **2018**, *8*, 11947.
112. Gale, J. D., Gulp: A Computer Program for the Symmetry-Adapted Simulation of Solids. *J. Chem. Soc., Faraday Trans.* **1997**, *93*, 629-637.
113. Gale, J. D.; Rohl, A. L., The General Utility Lattice Program (Gulp). *Molecular Simulation* **2003**, *29*, 291-341.

114. Matsui, M., A Transferable Interatomic Potential Model for Crystals and Melts in the System CaO-MgO-Al_2O_3-SiO2. *Mineralogical Magazine* **1994**, *58*, 571-572.

115. Minervini, L.; Zacate, M. O.; Grimes, R. W., Defect Cluster Formation in M_2O_3-Doped CeO_2. *Solid State Ion.* **1999**, *116*, 339-349.

116. Hinuma, Y.; Kamachi, T.; Hamamoto, N., Auto-Generation of Corrugated Nonpolar Stoichiometric Slab Models. *Mater. Trans.* **2020**, *61*, 78-87.

117. Pedregosa, F., et al., Scikit-Learn: Machine Learning in Python. *J. Mach. Learn. Res.* **2011**, *12*, 2825–2830.

118. Momma, K.; Izumi, F., Vesta 3 for Three-Dimensional Visualization of Crystal, Volumetric and Morphology Data. *J. Appl. Crystallogr.* **2011**, *44*, 1272-1276.

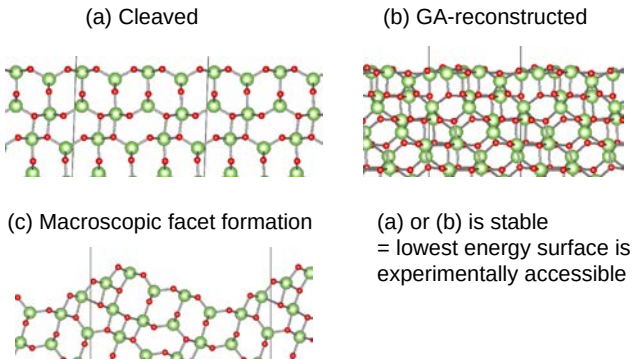
(a) Cleaved
(b) GA-reconstructed
(c) Macroscopic facet formation
(a) or (b) is stable
= lowest energy surface is
experimentally accessible

TOC figure